

A Reconstruction Method for Gappy and Noisy Arterial Flow Data

Alexander Yakhot*, Tomer Anor, and George Em Karniadakis

Abstract—Proper orthogonal decomposition (POD), Kriging interpolation, and smoothing are applied to reconstruct gappy and noisy data of blood flow in a carotid artery. While we have applied these techniques to clinical data, in this paper in order to rigorously evaluate their effectiveness we rely on data obtained by computational fluid dynamics (CFD). Specifically, gappy data sets are generated by removing nodal values from high-resolution 3-D CFD data (at random or in a fixed area) while noisy data sets are formed by superimposing speckle noise on the CFD results. A combined POD-Kriging procedure is applied to planar data sets mimicking coarse resolution “ultrasound-like” blood flow images. A method for locating the vessel wall boundary and for calculating the wall shear stress (WSS) is also proposed. The results show good agreement with the original CFD data. The combined POD-Kriging method, enhanced by proper smoothing if needed, holds great potential in dealing effectively with gappy and noisy data reconstruction of *in vivo* velocity measurements based on color Doppler ultrasound (CDUS) imaging or magnetic resonance angiography (MRA).

Index Terms—Carotid artery, computational fluid dynamics (CFD), kriging interpolation, proper orthogonal decomposition.

I. INTRODUCTION

THE RECENT advances in medical imaging have generated a lot of interest in developing *in vivo* techniques to obtain quantitative data for blood flow in arteries. Color Doppler ultrasound (CDUS) imaging is very effective in obtaining maps representing blood flow characteristics based on the Doppler principle. Magnetic resonance phase contrast (MR PC) velocity mapping methods encode the motion of flowing blood into the phase of the acquired signal. At the present time, there are still serious limitations in the spatial or temporal resolution of magnetic resonance imaging (MRI) and CDUS imaging. MRI is a 3-D technique for velocity imaging with high spatial resolution but low temporal resolution. Furthermore, it suffers from signal loss in turbulent flow, thus making it ineffective in imaging

stenotic arteries. CDUS imaging has very good temporal resolution but in conventional commercial ultrasound systems only the axial component of flow velocity can be estimated and visualized using the classic Doppler effect. To extend flow velocity estimation to two or three components, a number of techniques have been proposed [4], [5], [7], [11] but such systems require two or more transducers. However, the temporal resolution may be reduced by the occurrence of gappy regions if, for example, the imaged artery lies behind a bony structure. Several artifacts also occur during medical scanning, which may increase uncertainty in the data processing and lead to erroneous interpretations. Hence, part of the data may be discarded at some time instants due to being outside a prespecified confidence threshold. This may lead to spatial-temporal gappiness or, in some cases, part of the information may be totally missing due to shadowing (i.e., obstructed view), leading to the so-called “black zones.”

More specifically, the effects of artifacts in MR PC velocity imaging were considered in [29]. The authors studied cases when velocity displacement artifacts may register incorrect velocities to correct spatial locations. Spatial displacement artifacts may lead to a distortion of the lumen and velocities assigning the correct velocity field to incorrect spatial locations. Also, noise of different types and sources contaminates medical ultrasound (US) and MR imaging. For example, a US image is generated by reflected coherent ultrasound waves at fixed frequencies that interact with different tissue types and give rise to various interface phenomena causing speckle noise. In practice, speckle type is the dominant source of noise in US that should be filtered out [27].

Magnetic resonance angiography (MRA) is widely used for noninvasive and accurate acquisition of 3-D arterial geometries. Recently, a new technique, 3-D US was tested as an alternative to MRA for generating anatomically realistic 3-D geometric models [3]. The geometric model data is then exported into computational fluid dynamics (CFD) codes to obtain detailed description of the blood velocity field [23], [24], [26], [30]. It is believed that accurate CFD simulation of the blood flow can yield reliable quantification of the vessel wall shear stress (WSS), which plays a critical role in regulating the arterial structure [8], [12], [19]. Errors in image segmentation might affect CFD-based prediction of WSS. In [24], the authors considered the case of a straight cylindrical tube and performed CFD simulations based on a geometrical model obtained from magnetic resonance imaging (MRI). The computed WSS had errors up to 40%, however, a simple smoothing of the image boundary data reduced the errors to less than 16%. Time-resolved direct measurements of WSS remains a great challenge despite isolated successes using MRI or Doppler US methods (see [18], [25], [26], [31], [32], [35] and [2], [6], [14], respectively). Most

Manuscript received January 23, 2007; revised May 15, 2007. This work was supported in part by the National Science Foundation under Grant IMAG and Grant CI-TEAM and in part by the United States–Israel Binational Science Foundation under Grant 2001-150. *Asterisk indicates corresponding author.*

*A. Yakhot is with the Department of Mechanical Engineering, Ben-Gurion University of the Negev, Beersheva 84105, Israel (e-mail: yakhot@bgu.ac.il).

T. Anor was with the Department of Mechanical Engineering, Ben-Gurion University of the Negev, Beersheva 84105, Israel. He is currently with the Neurosurgery Department, Children’s Hospital Boston, Harvard Medical School, Boston, MA 02115 USA.

G. Em Karniadakis is with the Division of Applied Mathematics, Brown University, Providence, RI 02912 USA.

Color versions of some of the figures in this paper are available online at <http://ieeexplore.ieee.org>

Digital Object Identifier 10.1109/TMI.2007.901991

of these measurements have been restricted to the axial velocity component in a single plane or even in a single location. In [35], WSS derived from the 3-D MR PC velocity mapping measurements did not differ from the 2-D velocity measurements both *in vivo* or *in vitro*. Accurate estimation of WSS *vectors* requires accurate measurement of the near-wall velocity vector field and accurate identification of the vessel wall location. In [18], the near-wall velocity field was fitted by high-order polynomials in order to reduce the experimental data noise. The spatial derivatives of the fitted velocity yielded WSS while the vessel boundaries were obtained from the geometric model.

As a first step in a velocity reconstruction procedure, the aforementioned artifacts should be, if possible, identified and treated prior to using medical images for acquisition of clinical data. Therefore, the need exists for a robust strategy in obtaining reliable information from medical images. Fig. 1 shows an example of a real CDUS image, which is digitized prior to applying the procedure developed in this study. Specifically, the image of a common carotid artery (CCA) in Fig. 1(a) was obtained using the Philips HDI 5000 System. The CCA lumen was covered by 100 and 236 pixels in the axial and cross-sectional direction, respectively. The blood velocity is mapped using the red-green-blue (RGB) color specification. (We used the Matlab software to digitize RGB colors in order to obtain the velocity data.) Digitizing the image obtained by CDUS equipment [Fig. 1(a)] results in low-resolution velocity data, contaminated by noise. However, applying noise filtering and Kriging interpolation discussed in Sections II-D and II-C, respectively, improves the image considerably, as shown in Fig. 1(b). In addition, using the reconstruction procedure developed in this paper, we calculated the WSS shown in Fig. 1(c). Clearly, the results are visually improved compared to the original data but the question remains regarding their accuracy, since we do not have access to “finer” images and “true” results in order to evaluate the fidelity of this reconstruction technique.

To this end, in this paper we rely on 3-D CFD to generate imperfect data sets and address the issues of spatio-temporal gapiness and black zones. In addition, in order to consider other uncertainties that may affect the clinical data, we consider the effect of noise superimposed on the CFD results. We develop a procedure to reconstruct more accurate vector fields before any meaningful use or comparisons with computational predictions are made. For gappy data, including black zones, our approach employs the proper orthogonal decomposition (POD) based on the method of *snapshots* [10], [17] and on Kriging interpolation [28]. Specifically, for reconstruction of time-dependent *gappy* flow fields, we applied the extended POD approach presented in [33]. This method can be quite effective in exploiting redundancy in the measurements. For the regions of the domain in which data may be missing at *all* times (black zones) POD breaks down, so we employ Kriging interpolation which predicts unknown values (at known locations) from known values (at other known locations). Kriging is an effective statistical method, which has been used with success in geology to interpolate data scattered randomly in space. This method minimizes the error of predicted values by estimating the error from the spatial distribution of the predicted values. Unlike other estimation procedures, Kriging provides a measure of the error and of

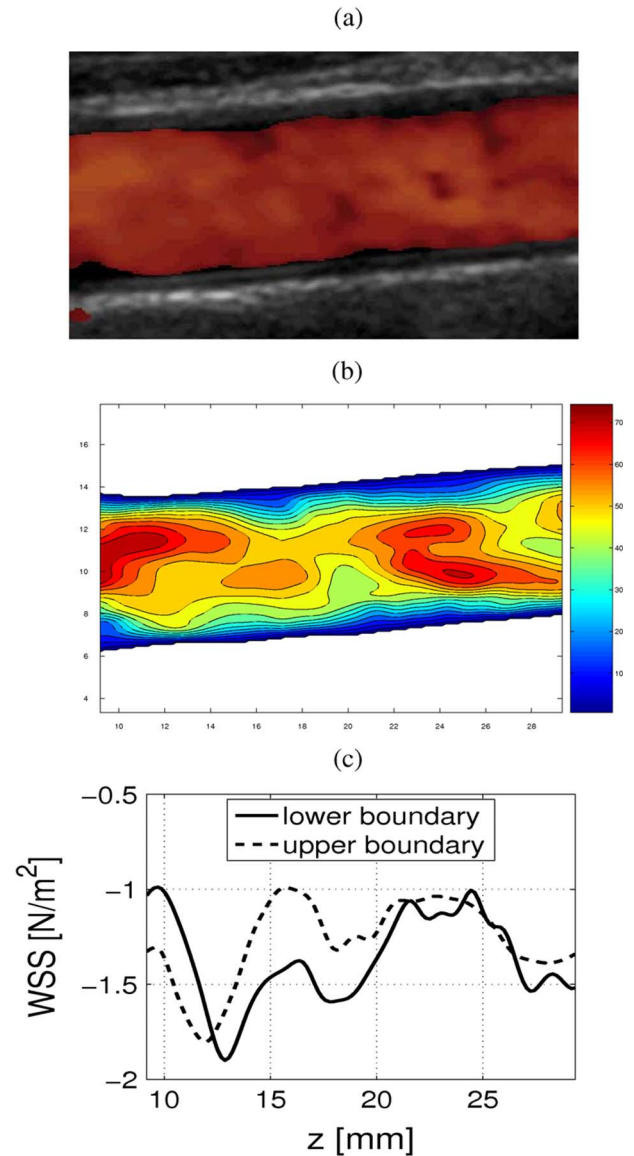


Fig. 1. (a) An *in vivo* CDUS flow image of the blood velocity in the CCA (courtesy of Prof. Y. Libson, and Dr. L. Appelbaum and Dr. T. Sella, Hadassah Medical Center, Jerusalem, Israel). Velocity field is mapped by RGB color specification. (b) Color map of the velocity after applying smoothing and Kriging interpolation. (c) Calculated WSS.

the associated confidence in the estimates. For noisy data we can also apply the POD approach—if snapshots from several cardiac cycles are available—in conjunction with smoothing of the hierarchical POD modes. If only the first mode (ensemble-mean field) is employed, then this is equivalent to obtaining the phase averaging of the ensemble of snapshots which corresponds to cardiac gating of data used to minimize motion artifacts.

The new methodology developed in the current work treats medical imaging data by the POD-Kriging (POD-K) procedure for quantitative clinical data extraction. We propose two basic advances towards the development of computer-aided tools for analyzing complex cardiovascular flows: 1) spatio-temporal reconstruction of the blood flow field based on medical images and 2) calculation of WSS. The objective of this study is to develop a method based on POD, Kriging interpolation, and smoothing for reconstruction of arterial flow data.

The paper is organized as follows. The theoretical aspects of the POD method are outlined in Sections II-A and II-B. In Sections II-C and II-D, we describe the Kriging interpolation and smoothing algorithm for noisy data. Formation of clinical data prototypes is explained in Section II-E. In Section III, we present the results of arterial flow data acquisition from gappy data and data with black zones (Section III-A) and from ultrasound-like noisy images (Section III-B). In Section IV, we discuss limitations and advantages of the developed method. Finally, in the Appendix we present details on the geometric model and on the CFD simulation.

II. METHODS

In the next two sections, we present an overview of the POD-based approach for gappy data and outline the Kriging procedure for black zones and for subpixel interpolation [13], [20]. Subsequently, we discuss smoothing of noisy data, and finally we describe how we generate clinical data prototypes and ultrasound-like noisy images from CFD results.

A. Proper Orthogonal Decomposition

We employ the following decomposition of a function $u(\mathbf{x}, t)$

$$u(\mathbf{x}, t) = \sum_{j=1}^m \phi_j(\mathbf{x}) a_j(t) \quad (1)$$

where $\mathbf{x} = (x, y, z)$, and $\phi_j(\mathbf{x})$ and $a_j(t)$ are the j th orthogonal spatial and temporal modes, respectively. The POD procedure yields the eigenfunctions $\{\phi\}$, which form the expansion basis in the above expression. Here, we implement the standard method of snapshots [10], [17] to obtain eigenfunctions and corresponding eigenvalues. Consider the collection of m data snapshots, $\{U^k\}_{k=1}^m$, where U^k is a vector containing the velocity field at time t_k for all $\mathbf{x} = \mathbf{x}_1, \dots, \mathbf{x}_N$, namely the elements of U^k are

$$u_i^k = u(t^k, \mathbf{x}_i), \quad i = 1, 2, \dots, N. \quad (2)$$

These snapshots are used to compute the POD basis vectors, which yield a representation of the data that is optimal in the sense that, for any given basis size, the L_2 norm of the error is minimized. This is equivalent to solving the eigenvalue problem

$$CA = \Lambda A \quad (3)$$

where the eigenvectors a_j (columns of the matrix A) represent the temporal modes, Λ is a diagonal matrix of the eigenvalues λ_j , and C is a correlation matrix formed by computing the inner product between every pair of snapshots U^i and U^k

$$C_{ik} = \frac{1}{m} (U^i, U^k), \quad i, k = 1, 2, \dots, m. \quad (4)$$

The magnitude of the j th eigenvalue λ_j represents the relative importance of the j th POD basis vector. This importance is commonly quantified by defining the relative energy content E_j for each basis vector j as

$$E_j = \frac{\lambda_j}{\sum_{k=1}^m \lambda_k}, \quad j = 1, 2, \dots, m \quad (5)$$

where the term ‘‘energy’’ refers to a measure in the L_2 norm. The j th POD basis vector, ϕ_j , is given by a linear combination of snapshots

$$\phi_j = \sum_{k=1}^m a_j^k U^k, \quad j = 1, 2, \dots, m \quad (6)$$

where a_j^k denotes the k th element of the j th eigenvector a_j . Finally, the reconstruction of the velocity field using $p \leq m$ modes is given by

$$\tilde{U}^k = \sum_{j=1}^p a_j^k \phi_j \quad (7)$$

for every $k = 1, 2, \dots, m$.

B. Gappy POD

This procedure was developed by Everson and Sirovich in [10] and can be described as follows [13]. The first step is to define a *mask vector*, which for a particular flow vector describes where data are available and where data are missing. For the flow solution U^k , the corresponding mask vector n^k is defined as follows:

$$n_i^k = \begin{cases} 0, & \text{if } u_i^k \text{ is missing} \\ 1, & \text{if } u_i^k \text{ is known} \end{cases} \quad (8)$$

for $i = 1, 2, \dots, N$ and $k = 1, 2, \dots, m$. Pointwise multiplication is defined as $(n^k, U^k)_i = n_i^k u_i^k$. Then the gappy inner product is defined as $(v, w)_n = ((n, v), (n, w))$, and the corresponding norm is $(\|v\|_n)^2 = (v, v)_n$.

Let $\{\phi_j\}_{j=1}^m$ be the standard POD basis for the snapshot set $\{U^k\}_{k=1}^m$, where all snapshots are completely known. Let $\{g^k\}_{k=1}^m$ be another set of solution vectors that have some elements missing, with corresponding mask vectors n_i^k . We want to reconstruct the full or repaired vector from the incomplete vectors $\{g^k\}_{k=1}^m$. Assuming that the vectors $\{g^k\}_{k=1}^m$ represent a solution whose behavior can be characterized with the existing snapshot set, the intermediate repaired vector $\{\tilde{g}^k\}_{k=1}^m$ can be expressed in terms of p POD basis functions as follows:

$$\tilde{g}^k \approx \sum_{j=1}^p b_j^k \phi_j, \quad k = 1, 2, \dots, m. \quad (9)$$

To compute the POD coefficients b^k , the error, ϵ , between the original and repaired vectors must be minimized. The squared error is defined as

$$(\epsilon^k)^2 = \|g^k - \tilde{g}^k\|_n^2, \quad k = 1, 2, \dots, m \quad (10)$$

using the gappy-norm so that only the original existing data elements in g are compared. The coefficients b_j^k that minimize the error ϵ^k can be found by differentiating (10) with respect to each of the b_j^k in turn. This leads to the linear system of equations

$$Mb^k = f^k, \quad k = 1, 2, \dots, m \quad (11)$$

where

$$M_{ij} = (\phi^i, \phi^j)_n, \quad i, j = 1, 2, \dots, m \quad (12)$$

and

$$f_j^k = (g^k, \phi_j)_n, \quad j, k = 1, 2, \dots, m. \quad (13)$$

Solving (11) for b^k and using (9), the intermediate repaired vectors $\{\tilde{g}^k\}_{k=1}^m$ can be obtained. Finally, the complete $\{g^k\}_{k=1}^m$ is reconstructed by replacing the missing elements in g^k by the corresponding repaired elements in \tilde{g}^k , i.e., $g_i^k = \tilde{g}_i^k$ if $n_i^k = 0$.

The initial condition used in the gappy region is typically the nonzero average value over all snapshots. A more robust version that does not depend on the initial guess and, in addition, enhances accuracy significantly was presented in [33]. The main steps of this iterative procedure are as follows.

Iterative Gappy POD (IG-POD):

- 1) Perform Gappy POD but employ only $p = 1$ modes in the reconstruction (9).
- 2) Use the result of the previous step as a new initial guess at the gappy points and apply Gappy-POD, but now employ $p = 2$ modes in the reconstruction.
- 3) Proceed similarly for the l -th iteration until the obtained eigenspectrum does not change anymore.

In [33], the authors suggest to employ two modes ($p = 2$) as the starting number of modes. However, in the present study, setting $p = 1$, as suggested in the algorithm above, leads to better accuracy.

C. Kriging Interpolation

We have adopted the Kriging interpolation method implemented in the Matlab toolbox DACE [20]. Let \mathcal{S} be composed of m known points, i.e., $\mathcal{S} = [s^{(1)}, s^{(2)}, \dots, s^{(m)}]$. A known value (response) of a function at those locations is denoted as $y_i = y[s^{(i)}]$. For example, y_i may be one of the three components of a velocity vector at point $s^{(i)}$. Let \mathbf{Y} be the vector containing all those responses, i.e., $\mathbf{Y} = [y_1, y_2, \dots, y_m]^T$. Let \mathcal{X} be composed of points x where the value of a function is *unknown*. The data is arranged in a matrix form and normalized, i.e., the mean of each vector (j th column in a matrix) is zero

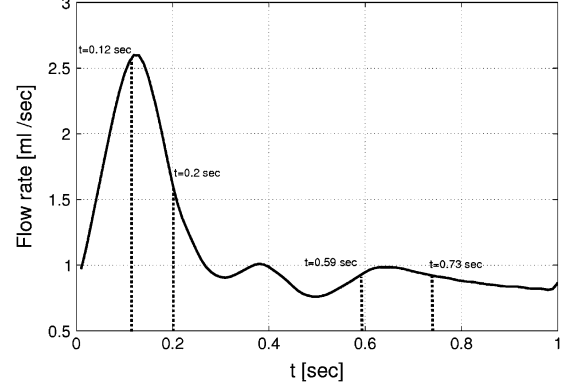


Fig. 2. Flow rate versus time. Marked times correspond to instants for which we perform the analysis although most results we present are for $t = 0.2$ s.

and the covariance is equal to unity. For the set \mathcal{S} of sampling points, we define the $m \times l$ interpolation matrix \mathbf{F} as

$$\mathbf{F}_{ij} = f_j[s^{(i)}] \quad (14)$$

where $f_p, p = 1, 2, \dots, l$, are l polynomial functions. In this study, the regression model is based on the second-order polynomials, and for any point x with coordinates (x, y, z) we have 10 polynomials. We also define the correlation $m \times m$ matrix \mathbf{R} by $\mathbf{R}_{ij} = R[\theta, s^{(i)}, s^{(j)}]$, where θ is the correlation parameter which is inversely proportional to the correlation length. The choice of correlation function should be based on the underlying phenomenon. Here, we restrict our attention to correlations which are products of stationary, 1-D correlation kernels, i.e., of the form

$$R[\theta, s^{(i)}, s^{(j)}] = \prod_{k=1}^3 R_k[\theta, s_k^{(i)}, s_k^{(j)}] \quad (15)$$

where k is a coordinate index. Then, the Kriging interpolation at an unknown point x is

$$\hat{y}(x) = \mathbf{f}(x)\mathbf{a} + \mathbf{r}^T(x)\mathbf{b} \quad (16)$$

where $\mathbf{f}(x) = [f_1(x), f_2(x), \dots, f_l(x)]$ is the interpolation $l \times 1$ matrix ($l = 10$ for the second-order polynomials regression model), and

$$\mathbf{a} = (\mathbf{F}^T \mathbf{R}^{-1} \mathbf{F})^{-1} \mathbf{F}^T \mathbf{R}^{-1} \mathbf{Y} \quad (17)$$

$$\mathbf{b} = \mathbf{R}^{-1} (\mathbf{Y} - \mathbf{F}\mathbf{a}) \quad (18)$$

when

$$\mathbf{r}(x) = \{R[\theta, s^{(1)}, x] \dots R[\theta, s^{(m)}, x]\}^T \quad (19)$$

is the vector of correlations. From (17) and (18), \mathbf{a} and \mathbf{b} are $l \times 1$ and $m \times 1$ matrices, respectively, obtained from the sampling points of \mathcal{S} .

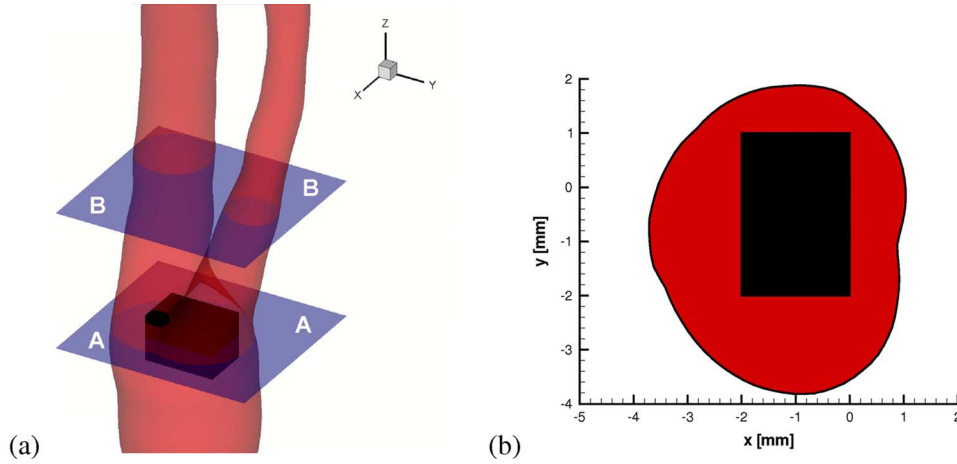


Fig. 3. (a) Carotid artery obtained from MRA; AA and BB are test sections where results are presented. (b) Black zone on the AA-plane.

We use the following correlation models between two points in space $\alpha_k, \beta_k, k = 1, 2, 3$.

- *Exponential kernel*:

$$R_k(\theta_k, \alpha_k, \beta_k) = \exp(-\theta_k |\alpha_k - \beta_k|). \quad (20)$$

- *Spline kernel*:

$$R_k(\theta_k, \alpha_k, \beta_k) = \psi(\xi_k). \quad (21)$$

where $\xi_k = \theta_k |\alpha_k - \beta_k|$ and

$$\psi(\xi_k) = \begin{cases} 1 - 1.5\xi_k + 0.5\xi_k^3, & \text{for } 0 \leq \xi_k \leq 0.2 \\ 1.25(1 - \xi_k)^3, & \text{for } 0.2 < \xi_k < 1 \\ 0, & \text{for } \xi_k \geq 1. \end{cases} \quad (22)$$

The correlation decreases with the distance between points $d_k = |\alpha_k - \beta_k|$, a larger value for θ_k leads to a faster decrease.

D. Smoothing Procedure

We applied smoothing to the temporal and spatial POD modes obtained from the noisy data after a preprocessing stage whereby ensemble-averaging of the available noisy data is performed. Specifically, we employ a locally weighted smoothing function, which is based on least squares quadratic polynomial fitting (LOESS), also known as locally weighted polynomial regression [9]. At each of the n points in the data set a low-degree polynomial is fit to a subset of the data, with independent variable values near the point whose response is being estimated. The polynomial is fit using weighted least squares, giving more weight to points near the point whose response is being estimated and less weight to points further away, i.e.,

$$w(x) = \begin{cases} (1 - |x|^3)^3, & \text{for } |x| < 1 \\ 0, & \text{for } |x| \geq 1. \end{cases} \quad (23)$$

The value of the regression function for the point is then obtained by evaluating the local polynomial using the independent variable values for that data point. The subsets of data used for each weighted least squares fit in LOESS are determined by a nearest neighbors algorithm. A user-specified input to the procedure called the “bandwidth” or “smoothing parameter” determines how much data is used to fit each local polynomial. The smoothing parameter, q , is a number between $(d + 1)/n$ and 1, with d denotes the degree of the local polynomial. The value of q is determined by the proportion of data used in each fit. The subset of data used in each weighted least squares fit is comprised of the nq (rounded to the next largest integer) points whose independent variables values are closest to the point at which the response is being estimated.

E. Formation of Clinical Data Prototypes From CFD Results

In order to have a reference basis for evaluating the accuracy of our method, we have performed 3-D CFD simulations of flow through a carotid artery. We used two different CFD codes based on finite volumes and spectral/hp element methods to verify the accuracy of the CFD results. The specific steps of the computational procedure are summarized in the Appendix.

1) *Gappy Data Sets*: The CFD results were used to create a sampling set \mathcal{S} of 101 snapshots for data reconstruction. Spatio-temporal gappiness was generated by randomly removing some nodal data in each snapshot. A measure of the “gappiness percentage” is defined for each snapshot as the ratio between the number of grid points (nodes) where the data is missing to the total number of nodes on that snapshot. In this study, the gappiness percentage is the same for all snapshots. In addition, we discarded the data from a spatially *fixed* region in all snapshots to create a “black zone,” as shown in Fig. 3(a); hereafter we will denote the black zone as \mathbb{X} .

2) *Ultrasound-Like Noisy Images*: Color flow mapping (CFM) represents flow velocities in different colors overlaid on the conventional B-mode (“Brightness”) anatomic images. However, the velocity computed from CFM images may not yield accurate results due to signal contamination with both random and colored noise. Here, we generate a clinical-like prototype by modifying the CFD results using relatively simple

noise models.¹ Specifically, we assume the noise to be random and uncorrelated with the clean (noise-free) image. The resulting ultrasound-like corrupted image can be described by

$$\mathbf{z} = \mathbf{s} + \mathbf{n} \quad (24)$$

where \mathbf{z} , \mathbf{s} , and \mathbf{n} are the corrupted image, denoised image, and the noise, respectively. In Fig. 16(c), we show an example of a noisy image obtained from the CFD results of a common carotid artery.

In practice, for clinical CDUS images, neither the denoised image \mathbf{s} nor the noise component \mathbf{n} is available. Here, in order to generate an ultrasound-like prototype of a clinical image, we consider the CFD results as the denoised image and we superimpose on it *speckle* noise, a special type of noise encountered in ultrasound B-mode data [1]. We assume that the speckle noise in (24) has nonzero mean *in time* but it has zero-mean *in space* for every snapshot, i.e., the resulting noise component is derived from

$$\mathbf{n}(t) = \tilde{\mathbf{n}}(t) - \text{space-mean}[\tilde{\mathbf{n}}(t)] \quad (25)$$

where $\tilde{\mathbf{n}}(t)$ is a Rayleigh random variable having probability density function

$$P(r) = \frac{r e^{-r^2/2s^2}}{2s^2} \quad (26)$$

for $r = [0, \infty)$ and the standard deviation $s = 1$.

Our goal is to develop a procedure, subject to certain criteria, for recovering the denoised image \mathbf{s} from (24) or to considerably reduce the noise \mathbf{n} . To estimate the noise level and evaluate the performance of the denoising procedure, we consider the *signal-to-noise-ratio* (SNR) and *noise-to-mean-ratio* (NMR). For each snapshot we define

$$\text{SNR} = \frac{\text{RMS}(\mathbf{z})}{\text{RMS}(\mathbf{n})}, \quad \text{NMR} = \frac{\text{RMS}(\mathbf{n})}{\text{mean}(\mathbf{z})}. \quad (27)$$

III. RESULTS

We first present reconstruction results for gappy data and black zones, and subsequently for noisy data. Hereafter, the axis units are given in [m] unless otherwise specified. Data analysis includes calculation of the velocity field, wall-shear stress, vessel wall location and comparison with the original (“true”) CFD results. In Sections III-A and III-B, we present results for different time instants marked in Fig. 2, where we show the waveform profile used as the inlet boundary condition for CFD simulations. We have chosen the planar views denoted by AA and BB in Fig. 3 for demonstration purposes.

¹Some experimental measurements employ signal-dependent noise model, e.g., $\mathbf{z} = \mathbf{s} + \sqrt{\mathbf{s}}\mathbf{n}$ in [22], which is beyond of the scope of the present study.

TABLE I

CASE STUDIES AND POD-KRIGING PROCEDURE. S: SAMPLING DATA; X: BLACK ZONE DATA; “KRIGING IN S” MEANS GRID REFINEMENT; HRX: HIGH-RESOLUTION CFD DATA WITH A HOLE; HRGX: HIGH-RESOLUTION CFD DATA WITH A HOLE AND 50% GAPPINESS; LRG: LOW-RESOLUTION CFD DATA WITH 50% GAPPINESS; LRGX: LOW-RESOLUTION CFD DATA WITH A HOLE AND 50% GAPPINESS

Grid	High Resolution		Low Resolution	
	S complete	S gappy	S complete	S gappy
Black zone	X	X		X
Abbrev.	HRX	HRGX	LRG	LRGX
Step 1	Kriging in X	POD in S	POD in S	POD in S
Step 2	Data analysis	Kriging in X	Kriging in S	Kriging in X
Step 3		Data analysis	Data analysis	Kriging in S
Step 4				Data analysis

TABLE II

TIME-AVERAGED ERROR (TARMS) (%) OF THE VELOCITY FIELDS RECONSTRUCTED FROM THE CFD DATA WITH DIFFERENT NUMBER OF POD MODES. HRX: HIGH-RESOLUTION CFD DATA WITH A HOLE; HRGX: HIGH RESOLUTION CFD DATA WITH A HOLE AND 50% GAPPINESS

Original data	j , number of POD modes						
	1	2	3	4	6	8	10
$\epsilon_u^{(j)}$, CFD	13.66	6.55	3.50	1.83	0.93	0.57	0.32
$\epsilon_u^{(j)}$, HRX	13.69	6.61	3.65	2.08	1.36	1.14	1.04
$\epsilon_u^{(j)}$, HRGX	13.69	6.61	3.65	2.08	1.36	1.14	1.04
$\epsilon_v^{(j)}$, CFD	14.63	7.52	3.60	1.87	0.91	0.54	0.38
$\epsilon_v^{(j)}$, HRX	14.82	7.78	4.11	2.73	2.18	2.05	2.01
$\epsilon_v^{(j)}$, HRGX	14.82	7.78	4.11	2.73	2.18	2.05	2.01
$\epsilon_w^{(j)}$, CFD	8.38	4.81	1.94	0.96	0.43	0.23	0.14
$\epsilon_w^{(j)}$, HRX	8.39	4.82	1.96	1.00	0.53	0.39	0.34
$\epsilon_w^{(j)}$, HRGX	8.39	4.82	1.96	1.01	0.53	0.39	0.34

A. Gappy Data and Black Zones

We have performed our analysis for various time instants but here we present results corresponding to $t = 0.2$, i.e., during the decelerating phase (see Fig. 2), as numerical simulations revealed regions of reverse flow at that instant. In Table I, we summarize all cases considered and the steps of the flow data reconstruction procedure. High-resolution (HR) data were used for a 3-D velocity field while low resolution (LR) data were especially created using a coarse computational mesh to mimic ultrasound 2-D data. Gappiness (G) and a black zone (X) were introduced in *ad hoc* fashion to create more demanding data reconstruction scenarios.

1) *High-Resolution Gappy Data With a Black Zone*: In this section, we present the results of the first two cases of Table I, HRX and HRGX. A sketch of the black zone in the test cross-section is shown in Fig. 3(b). In the first case (HRX), the missing data in the black zone X are recovered by Kriging interpolation. In the second case (HRGX), the gappiness is 50%. The first step is to complete the gappy data S by the iterative gappy POD (IG-POD) algorithm described in Section II-B. Then, we perform the same steps as in the HRX case.

The normalized eigenvalue of a single POD mode represents its contribution to the total kinetic energy of the field. For the laminar flow considered in this paper, the first two modes contain most of the energy ($> 99\%$), but as will be shown below, that does not mean that the velocity field could be reconstructed with the same accuracy using only the first two modes. Let the

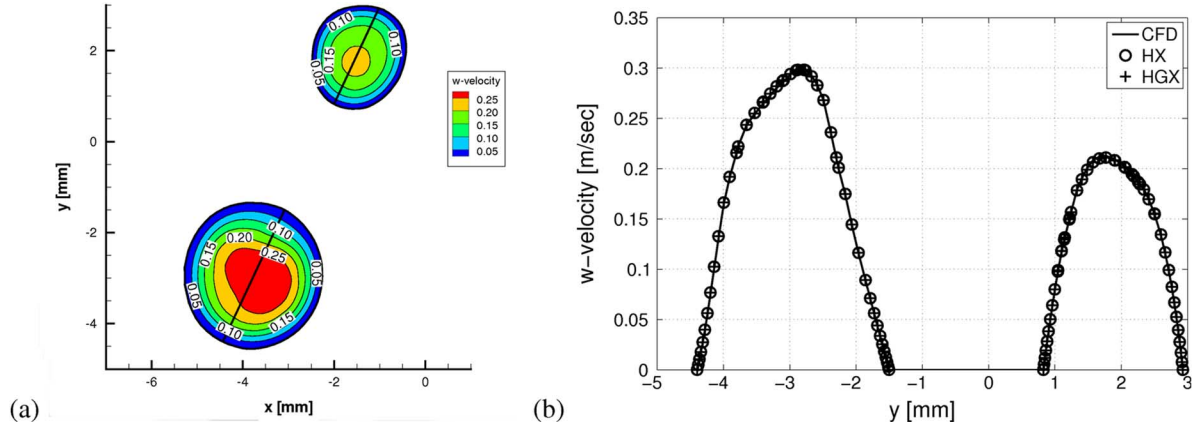


Fig. 4. Test-section BB [see Fig. 3(a)]: comparison of the complete and reconstructed sets in terms of the first three POD modes of the w -velocity field, $t = 0.2$. (a) Complete CFD data. (b) w -velocity profile along the line shown in (a). HRX denotes a black zone, HRGX denotes 50% gappiness and a black zone.

time-averaged error of the velocity fields reconstructed from the CFD data set with different number j ($j \leq M$) of POD modes be

$$\epsilon_u^{(j)} = \sqrt{\frac{1}{M} \sum_{i=1}^M \frac{\int_{\Omega} (u_i - u_i^{(j)})^2 d\Omega}{\int_{\Omega} u_i^2 d\Omega}} \quad (28)$$

where the subscript i is the snapshot number, the subscript j refers to number of POD modes used for reconstruction, u_i and $u_i^{(j)}$ are the u -component of the velocity fields known from the CFD simulation and reconstructed by POD, respectively; $\epsilon_v^{(j)}$ and $\epsilon_w^{(j)}$ are defined in a similar fashion. The time-averaged error represents the time-averaged root-mean-square (TARMS) of the difference between the original CFD-based velocity field and that reconstructed by POD. In Table II, we summarize the time-averaged errors for different cases. We note that TARMS asymptotically decreases towards a minimal bound ϵ_{\min} by increasing the number of POD modes. Clearly, ϵ_{\min} is determined by the gappiness percentage, the location of gappy sites and also by the size and location of the black zone; in Table II, we include TARMS results up to mode $j = 10$. We see that in order to reproduce all three velocity components with an error less than 5% or 2% we must use 3 or 10 POD modes, respectively. We also note another feature demonstrated in Table II, that the error in the streamwise component $\epsilon_w^{(j)}$ is less than $\epsilon_u^{(j)}$ and $\epsilon_v^{(j)}$. This can be attributed to the fact that the streamwise w -velocity is more coherent with much larger *mean* value than the cross-flow u - and v -components.

Fig. 5 shows the POD eigenspectrum of the reconstructed velocity field. The difference with the eigenvalues of the true CFD-based field (also shown in Fig. 5 for comparison) is very small. To recover the missing data in the black zone, we apply Kriging interpolation with the exponential kernel defined in (20). The black zone is embedded within a larger region, so that it is surrounded by known data points. Kriging interpolation is then applied on this extended region. We have found that in this case applying the POD procedure prior to a black zone recovery by Kriging enhances the accuracy.

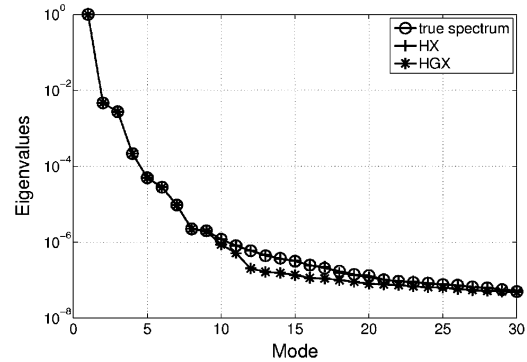


Fig. 5. Eigenvalues obtained from POD analysis of different CFD data.

The corresponding TARMS errors for HRX and HRGX cases are summarized in Table II. For the CFD data, the TARMS error asymptotically decreases to zero as the number of POD modes increases. For data with a hole, Kriging interpolation introduces small overall errors, which converge asymptotically to about 1.01%, 1.99%, and 0.32% for the u -, v -, and w -velocity components, respectively. The relative error of the streamwise w -velocity calculated in the black zone varied between 3.5%–6.5% for all times. The corresponding error ranges for the u - and v -velocity were larger, namely 7%–10% and 13%–21%, respectively. From Table II, we see that the HRX and HRGX errors are almost identical (within two-digit accuracy) because the hole size was the same in both cases and the 50% gappiness recovered by the IG-POD procedure does not introduce any noticeable additional inaccuracies.

Fig. 6(a) shows the original complete w -velocity field obtained at the cross-section AA, just upstream of the bifurcation. In Fig. 6(b), we show this field after randomly removing 50% of the data and discarding the data in the black zone. In Fig. 6(c), we present the field shown in Fig. 6(b) after POD-K reconstruction using all POD modes. Fig. 6(d) shows the field reconstructed from the CFD data with a hole (HRX case). Comparing Fig. 6(a) and c shows remarkable similarity except the core region wherein the Kriging interpolation in the black zone was performed prior to POD. From the “true” data shown in Fig. 6(a), there are two regions exhibiting near-wall reverse flow,

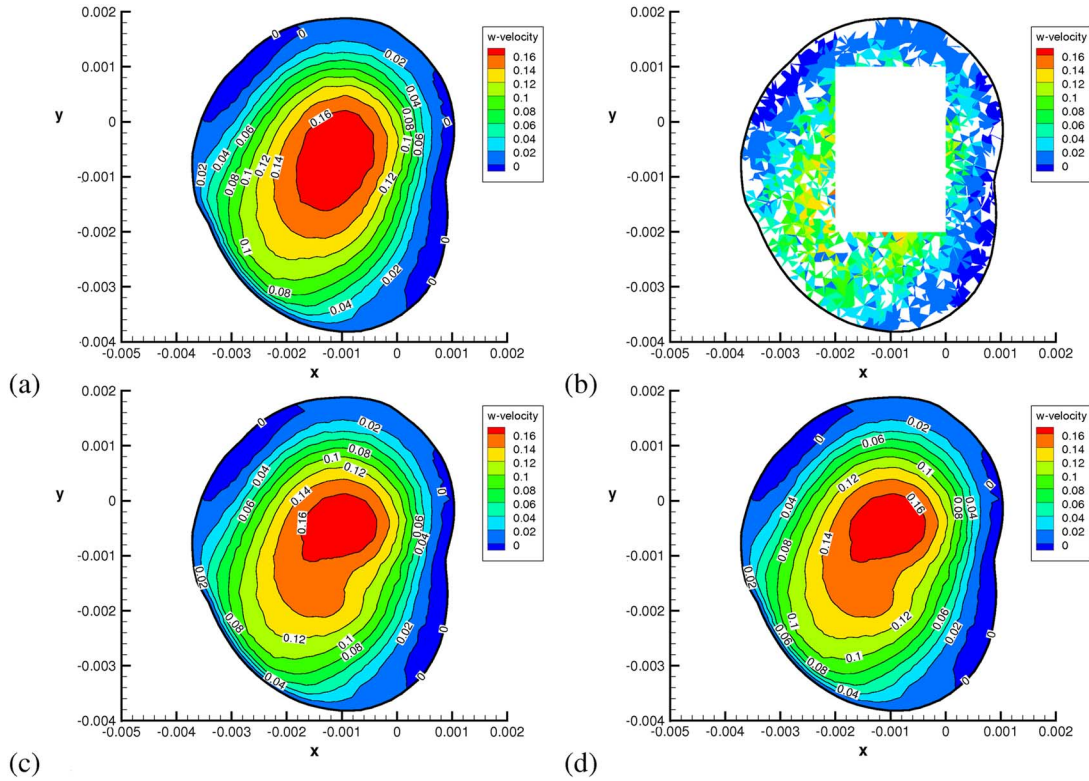


Fig. 6. Test-section AA: Comparison of the CFD-based and reconstructed by all POD modes w -velocity field at $t = 0.2$. Contours labeled with zero indicate back-flow regions with negative velocity. (a) Complete CFD data, (b) 50% gappiness and a black zone (hole) (HRGX), (c) the field in Figs. 6(b). After reconstruction, (d) the field reconstructed from the CFD data with a black zone (HRX).

and one can expect that such regions may be most complicated for the reconstruction. Nevertheless, the overall accuracy estimated by the TARMS error (see Table II) shows very good agreement with the original field. We note that comparison of the field shown in Figs. 6(a) with one reconstructed with the first three POD modes showed negligible difference in the details of the near-wall back-flow region.

To show the influence of the black zone on the flow reconstruction downstream of the location of the missing data in the bifurcation region, we illustrate in Fig. 4(a) the velocity field obtained at the cross-section BB. Fig. 4(b) presents a more quantitative comparison of the w -velocity profiles along the two lines shown in Fig. 4(a). Again, the difference between the HRX and HRGX cases is negligible. Fig. 4 and 6, along with the TARMS errors listed in Table II—which are remarkably low—demonstrate clearly that the missing data have been effectively recovered by Kriging interpolation.

2) Low-Resolution Gappy Data Without/With a Black Zone:

In this section, we consider cases LRG and LRGX of Table I. We presume that after acquisition of the clinical data some unreliable data (in accordance with certain criteria) may have been discarded, and thus the images are of low spatial resolution with gappy (missing) data. In practice, a more realistic scenario is to assign continuous *confidence levels* (from zero to one) to data at each location instead of zero or one for missing points or points for which information is known *for sure*, respectively. However, for the purposes of the comparative study presented here, we separate the effect of gappiness considered in the current section from the effect of noise, which we study in Section III-B.

We start by assuming that clinical CDUS images have low spatial resolution and that only the w streamwise velocity component is available. In Fig. 7, we show 2-D axial slices selected for synthesizing an ultrasound-like image from the CFD data set. The slice in Fig. 7(a) has been chosen to include the stenosed region of the internal carotid (ICA) where reverse flow may occur during some phases of a cardiac cycle. The slice in Fig. 7(b) intersects a bifurcation region and contains the carotid bulb where the flow usually exhibits complex behavior. In Fig. 7(a), the vessel boundaries are marked by Xa and Xb . To create an ultrasound-like image, we first export (interpolate) the high-resolution CFD data from the selected plane onto a coarse rectangular mesh (*Mesh 1*) shown in Fig. 8(a). The magnified view of the near-wall region in Fig. 8(a) illustrates the number of the (computational) grid lines that have been skipped upon interpolating the true (CFD) field. A typical in-plane spatial resolution for both MRI and CDUS is about $500 \mu\text{m}$ [23] but in-plane resolutions of $310 \times 310 \mu\text{m}^2$ have recently become available [35]. *Mesh 1* is equally-spaced in each direction with resolution $\Delta x = 140 \mu\text{m}$, $\Delta z = 130 \mu\text{m}$, which is somewhat beyond the limit of currently used CDUS devices. Thus, the low-resolution image created on *Mesh 1* is supposed to mimic a real-life CDUS image. To synthesize even more severe scenarios when an image is corrupted due to technical reasons, we randomly discarded some data to create a 50% gappiness [see Fig. 12(b) and Fig. 13(b)]. In addition, we assume the presence of a black zone shown in Figs. 12(b) (LRGX case in Table I) where the information is missing at all times.

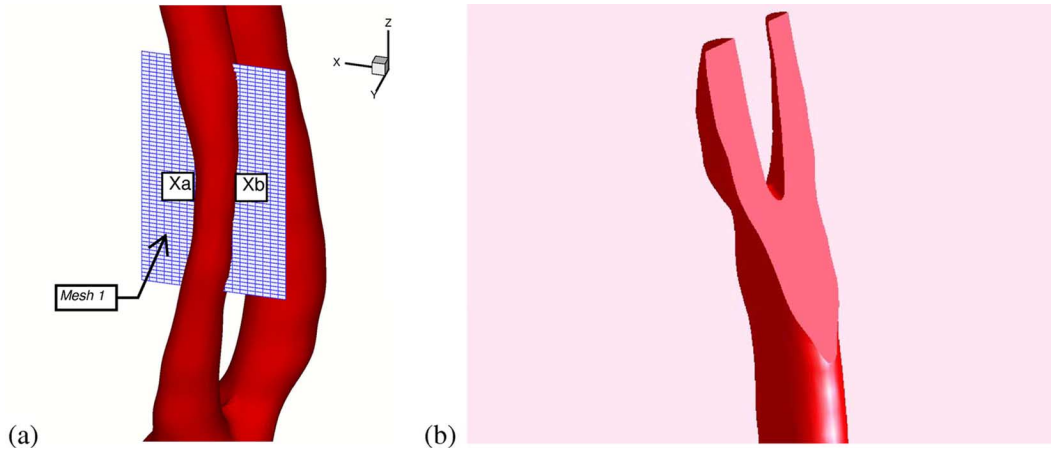


Fig. 7. Test slices for formation of ultrasound-like images. (a) Stenosed region of ICA; Xa and Xb denote the vessel boundaries. (b) Bifurcation region.

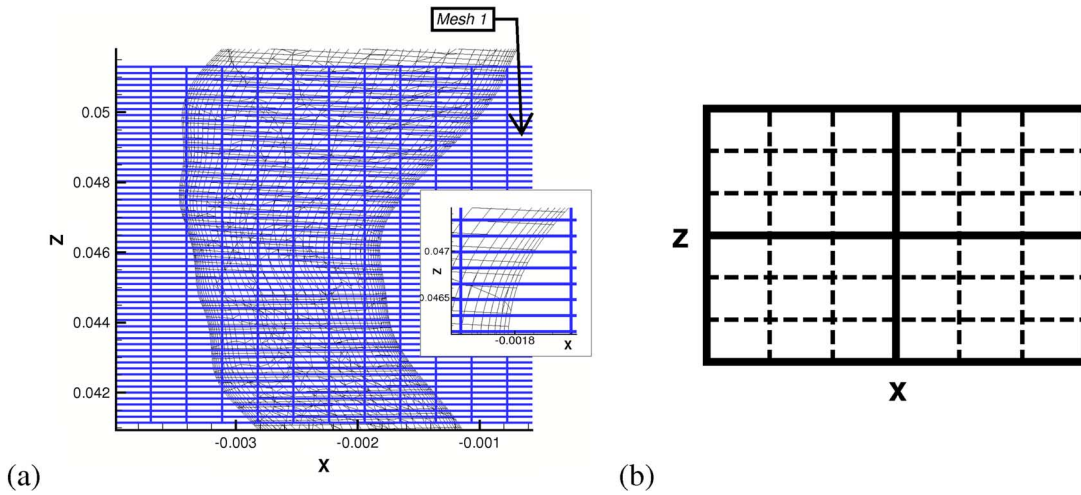


Fig. 8. (a) Numerical data are transferred onto rectangular mesh (*Mesh 1*). (b) Kriging interpolation is performed on *Mesh 2*: dashed line (*Mesh 1*: solid line).

The POD-Kriging procedure for the LRG case (an ultrasound-like image) consists of two steps listed in Table I. The first step is the gappiness elimination by implementing the IG-POD procedure described in Section II-B. This results in a complete data set defined on a coarse *Mesh 1* for each snapshot. The second step is refinement of an ultrasound-like image. To this end, the low-resolution *Mesh 1* is refined to create *Mesh 2*. In our simulations, *Mesh 2* has three times higher resolution than *Mesh 1* in each direction, i.e., $\Delta x = 47 \mu\text{m}$, $\Delta z = 43 \mu\text{m}$ [see Fig. 8(b)]. The missing (subgrid or subpixel) data of the *Mesh 2* are recovered using the Kriging interpolation with the *spline kernel* defined in (21). The reconstruction procedure for the LRGX case consists of three steps, when the Kriging interpolation is performed twice: first, to reconstruct the data in the black zone \mathbb{X} , and, second, to interpolate the data from *Mesh 1* to *Mesh 2*.

In Figs. 12 and 13, we show the w -velocity reconstructed on the test slices shown in Fig. 7 by applying the POD-K procedure. We recall that the true (CFD) velocity field was obtained on a high-resolution unstructured grid while the ultrasound-like images were designed by interpolating this field onto the low resolution rectangular *Mesh 1*. As a result, the vessel boundary of

the reconstructed image is unresolved [saw-like, see Fig. 12(c) and Fig. 13(c)]. To quantify the accuracy of the data reconstruction, we computed the RMS error defined by

$$\text{rms}^{(w)} = \sqrt{\frac{\int_{\Omega} (w - \tilde{w})^2 d\Omega}{\int_{\Omega} w^2 d\Omega}} \quad (29)$$

where \tilde{w} is the velocity reconstructed on the refined mesh *Mesh 2* and w is the “true” CFD-based velocity interpolated onto the same *Mesh 2*. For the stenosed part of the ICA shown in Fig. 12(a), $\text{rms}^{(w)} = 0.48\%$ and 1.09% for the LRG and LRGX cases, respectively, while for the bifurcation region, Fig. 13(a), $\text{rms}^{(w)} = 1.6\%$. The presented values are overall RMS errors computed for the entire domain Ω shown in Fig. 12. The local RMS, computed for a subdomain $x \geq -0.002, z \geq 0.049$, are 0.52% and 0.56% for the low-resolution LRG and LRGX cases, respectively. The local RMS computed for the black zone is 2.06% . The number of POD modes—chosen by the iterative IG-POD procedure in accordance with the convergence criterion, as described in Section II-B—varied from 20 to 30.

3) *Vessel Wall Location and WSS*: The Kriging interpolation gives an *analytical* approximation of the field $\tilde{w}(x, z) =$

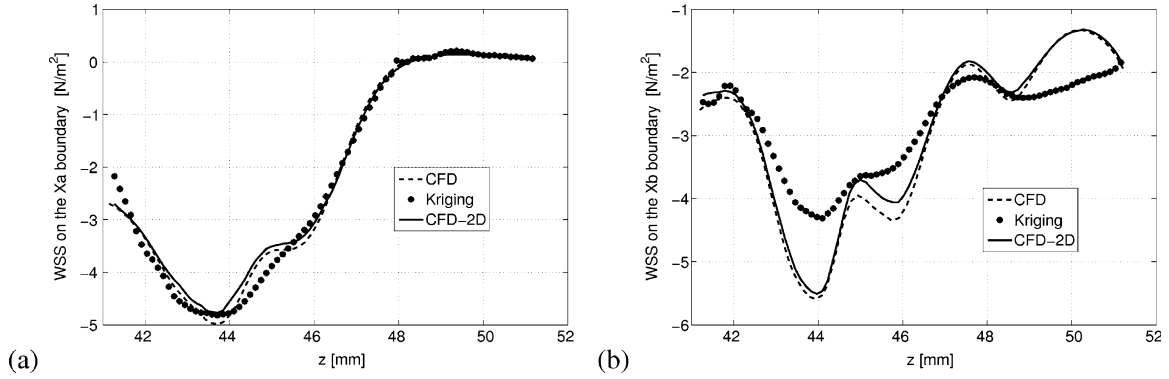


Fig. 9. *Mesh 1*, $t = 0.2$. Calculation of WSS from an ultrasound-like image with spatial resolution $\Delta x = 140 \mu\text{m}$, $\Delta z = 130 \mu\text{m}$, 50% gappiness and a black zone. WSS: symbols—POD-Kriging, solid line—CFD, (32), dashed line—CFD, (33). (a) Xa-boundary. (b): Xb-boundary.

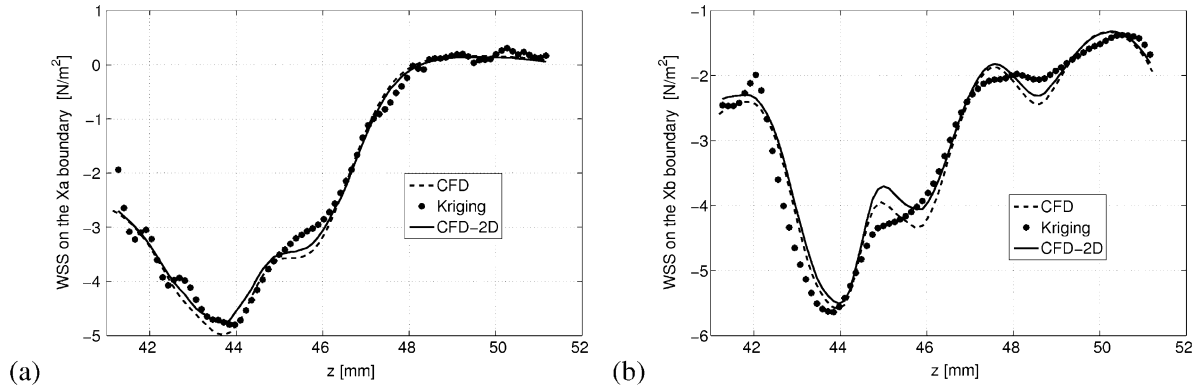


Fig. 10. Same as in Fig. 9 but for enhanced resolution towards the vessel's wall, $\Delta x = 93 \mu\text{m}$.

$\mathbb{K}(w)$. This is an obvious advantage, since $\tilde{w}(x, z)$ is *continuous* and *differentiable*, and can be used for 1) finding the vessel boundary location from $\tilde{w}(x, z) = 0$, and 2) computing the WSS. Accurate estimation of WSS requires accurate identification of the vessel's boundary. The true (CFD) and reconstructed boundaries are shown in Fig. 11. The most difficult area for reconstruction is the region of $48 < z < 51$. This region is characterized by very low velocity and possible reverse flow [marked by arrow in Fig. 12(a)]. Hence, special attention should be paid to the surface where the reconstructed velocity field is zero, $\tilde{w}(x, z) = 0$, in order to identify accurately the correct boundary. From Fig. 11, the agreement between the true and reconstructed boundaries is very good.

The viscous stress tensor τ_{ij} of a Newtonian fluid is defined by $\tau_{ij} = \mu(\frac{\partial u_i}{\partial x_j} + \frac{\partial u_j}{\partial x_i})$, where μ is the dynamic viscosity and $\mathbf{u} = (u, v, w) \equiv (u_i, i = 1, 2, 3)$ are velocity components. For flows in complex geometry, the local wall shear stress $\vec{\tau}_{\text{wall}} = (\tau_x, \tau_y, \tau_z) \equiv (\tau_i, i = 1, 2, 3)$ is defined to be proportional to the rate of change of the velocity in the direction normal to the wall, i.e., $\tau_i = \mu \frac{\partial u_i}{\partial x_j} n_j$. For example, for a 2-D flow in the (x, z) -plane, $\mathbf{u} = (u, 0, w)$, $(\partial)/(\partial y) = 0$, and we have

$$\vec{\tau}_{\text{wall}} = \mu \left(\frac{\partial u}{\partial x} n_x + \frac{\partial u}{\partial z} n_z, 0, \frac{\partial w}{\partial x} n_x + \frac{\partial w}{\partial z} n_z \right). \quad (30)$$

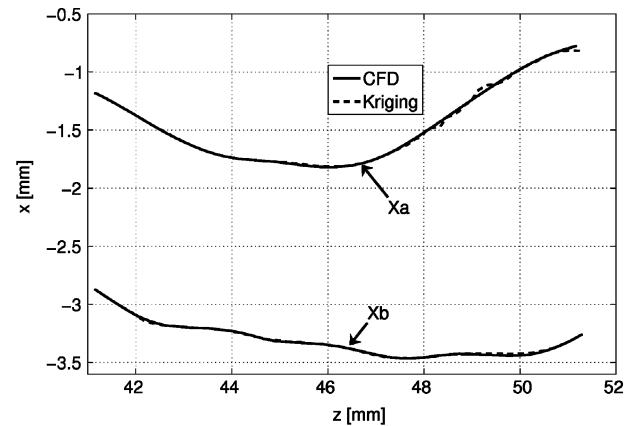


Fig. 11. Comparison of the true (CFD) vessel's boundary with that reconstructed by the Kriging procedure.

The two-dimensional character of an ultrasound image dictates certain limitations in computing WSS². In particular, we must assume that the flow is independent of the direction perpendicular to the image plane. In addition, a typical CDUS image provides only one velocity component (in our case, the stream-wise component w). Therefore, for calculation of WSS for the

²The described procedure is general and can be applied to 3-D images obtained by CDUS or MRI.

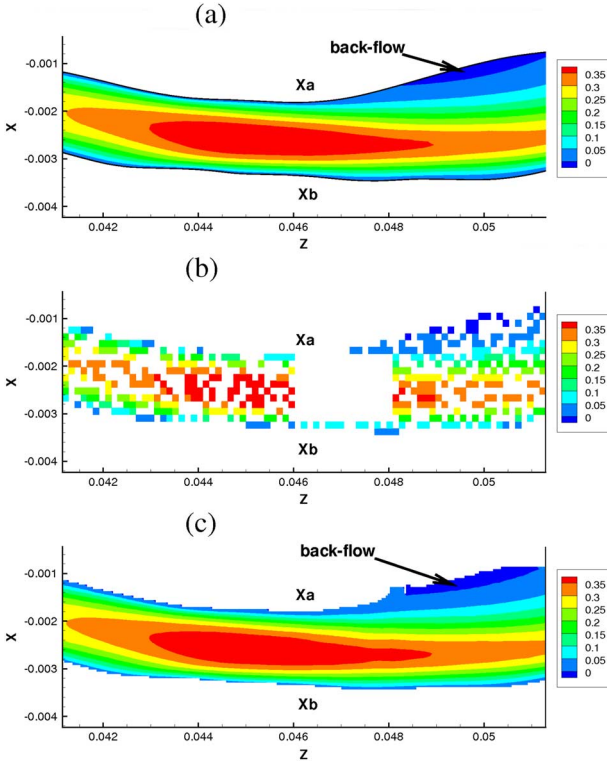


Fig. 12. Reconstruction of the axial w -velocity field, $t = 0.2$. (a) CFD: an arrow shows a back-flow region with negative velocity. (b) An ultrasound-like image, *Mesh 1*, 50% gappiness with a black zone (hole). (c) Image shown in (b) after POD-K.

synthesized CDUS image considered in this paper, we used the following approximation

$$\text{WSS} = \mu \left(\frac{\partial \tilde{w}}{\partial x} n_x + \frac{\partial \tilde{w}}{\partial z} n_z \right). \quad (31)$$

The partial derivatives $(\partial \tilde{w})/(\partial x)$, $(\partial \tilde{w})/(\partial z)$ are calculated analytically; on the boundary, their values are computed under the constraint $\tilde{w}(x, z) = 0$. For the CFD data, the wall shear stress was computed by two different ways

$$\text{WSS}_{\text{CFD-2D}} = \mu \left(\frac{\partial w}{\partial x} n_x + \frac{\partial w}{\partial z} n_z \right) \quad (32)$$

and

$$\text{WSS}_{\text{CFD}} = \mu \left(\frac{\partial w}{\partial x} n_x + \frac{\partial w}{\partial y} n_y + \frac{\partial w}{\partial z} n_z \right). \quad (33)$$

Using the expression in (32) is more appropriate for the ultrasound-like image considered in this study because (33) requires the derivative along the direction perpendicular to the image, which is assumed to be unavailable from a typical 2-D CDUS image. Figs. 9 and 10 show a comparison of the WSS calculated after applying the POD-Kriging procedure for the ultrasound-like image. In Fig. 9, we show results obtained on the coarse *Mesh 1* with $\Delta x = 140 \mu\text{m}$, $\Delta z = 130 \mu\text{m}$. The WSS on the lower Xb-boundary is affected by its “wavy” form (see Fig. 11)

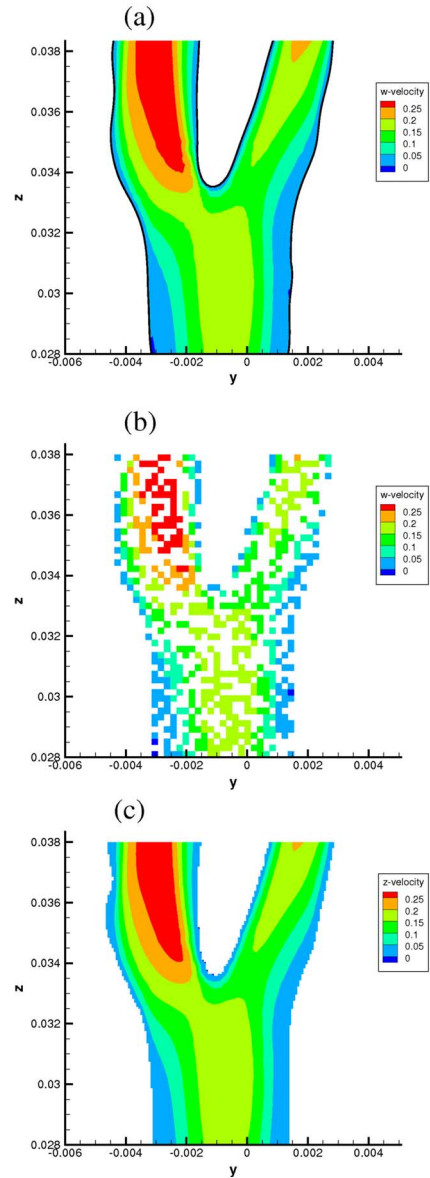


Fig. 13. Reconstruction of the axial w -velocity field in the bifurcation region, $t = 0.2$; (a)—CFD; (b)—an ultrasound-like image, low resolution *Mesh 1*, 50% gappiness; (c)—the image shown in (b) after POD-K.

which could not be properly captured on the coarse *Mesh 1*. The results in Fig. 10 were obtained on a similar mesh but refined by a factor of 1.5 along the x direction, i.e., $\Delta x = 93 \mu\text{m}$. The improvement of the WSS computed on the Xb-boundary with slightly finer mesh is significant and it points to the sensitivity of WSS calculation. The relative errors are summarized in Table III.

B. Noisy Data

In this section, we present the results of noisy data reconstruction by applying the POD-Kriging procedure enhanced with ensemble or phase averaging and smoothing of the noisy POD modes. In particular, we use the same CFD results as before by taking 101 snapshots of the w -velocity field for a selected part of the CCA. Fig. 16(a) shows the snapshot at $t = 0.2$ at a cross-section shown in Fig. 7(a). Speckle (Rayleigh) noise with

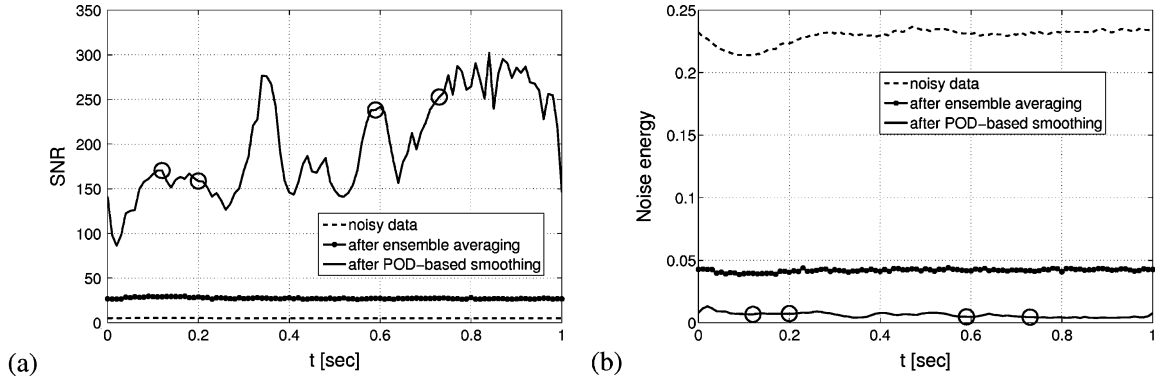


Fig. 14. SNR (a) and noise energy (b); open circles indicate the time instances when the WSS was computed.

TABLE III
RELATIVE ERRORS BETWEEN COMPUTED WSS
AND THE “TRUE” WSS_{CFD-2D} ($t = 0.2$)

Boundary	Mesh 1	Mesh 2
Xa	6.8%	6.3%
Xb	18.9%	8.5%

TABLE IV
RELATIVE (PERCENTAGE) ERRORS IN RECONSTRUCTING TEMPORAL
($\epsilon_a^{(j)}$) AND SPATIAL ($\epsilon_\phi^{(j)}$) POD MODES OF NOISY DATA

POD modes	j , number of POD modes			
	1	2	3	4
$\epsilon_a^{(j)}$	0.9	1.5	6.0	15.4
$\epsilon_\phi^{(j)}$	0.3	2.8	15.4	19.2

nonzero mean was added at each grid point of the snapshot [see Fig. 16(b)], with SNR ($\text{SNR} \approx 5$). This procedure was repeated 30 times yielding 30 realizations (ensemble). A sample of the noisy flow field is shown in Fig. 16(c). In practice, this ensemble can be obtained from a single measurement over 30 cardiac cycles in which not every one is identical due to either uncertainties in measurements or due to pathological effects of a diseased artery.

1) *POD Noisy Modes*: The ensemble-mean velocity field, $\langle w(\mathbf{x}, t) \rangle$, can now be decomposed further in *space-time* using the POD procedure described in Section II-A as follows:

$$\langle w(\mathbf{x}, t) \rangle = \sum_{i=1}^{M=101} a_i(t) \phi_i(\mathbf{x}). \quad (34)$$

However, the field $\langle w(x, z, t) \rangle$ is still noisy [see Fig. 16(d)] because the added speckle noise has *nonzero* ensemble-mean. We note that the shape of the first temporal mode, $a_1(t)$, resembles the flow rate and is affected little by the added noise compared to the higher modes, consistent with the hierarchical nature of the POD representation. In contrast to the temporal modes, all *spatial* modes are noisy as they are obtained from (6) which employs the *noisy* velocity field, see Fig. 16(d)

The normalized POD eigenspectrum is plotted in Fig. 15 and shows relatively smaller contribution of the third and fourth modes to the final field. It is also clear that the POD modes with index $m \geq 5$ do not contribute at all to the reconstruction after the ensemble averaging is performed.

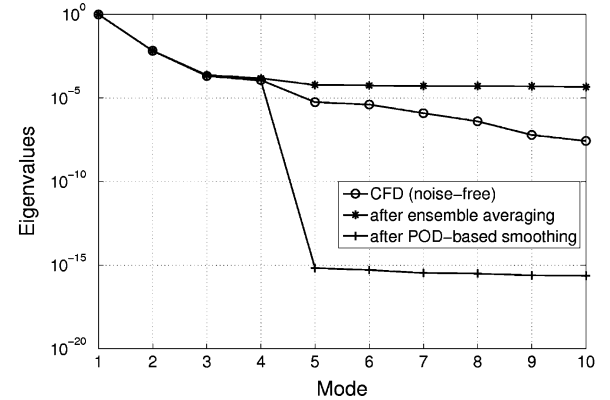


Fig. 15. Eigenvalues of the w -velocity POD modes of the CFD data (noise-free), ensemble-averaged and reconstructed by POD-Kriging procedure data.

As the final step of the denoising procedure, the spatial and temporal POD modes are smoothed using the smoothing method described in Section II-D. The relative reconstruction errors of the first four modes are summarized in Table IV. The values in Table IV deserve some comments. Due to the hierarchical nature of the POD modes, the amplitudes of the higher modes are very small, so that even small amounts of noise may totally corrupt the modes rendering them unrecoverable. Therefore, the POD expansion should be truncated since the corrupted tail would only introduce noise to the final field. Such truncation corresponds to simple cutoff filtering. In our simulations, the number of modes chosen for the POD reconstruction is $\tilde{M} = 4$ since it yields the maximum SNR.

In Fig. 14, we plot SNR and NMR before and after the POD-based smoothing. The initial $\text{SNR} \approx 5$ of the noisy data was increased to about 25 after the ensemble averaging. The level of the initial noise is about 22% of the velocity mean value. The final SNR ranges between $100 < \text{SNR} < 300$ indicating the effectiveness of the applied procedure. Finally, the color map of the reconstructed velocity is shown in Fig. 16.

2) *Vessel Wall Location and WSS*: We repeated the calculation of the WSS described in Section III-A.3 but for the noisy data for four time instants as indicated in Figs. 2 and 14. The time $t = 0.12$ is close to the peak systolic phase while $t = 0.2$ to the deceleration phase with reverse flow present in the ICA in the vicinity of the stenosis throat. The flow field for these two specific time instants are particularly difficult for flow recon-

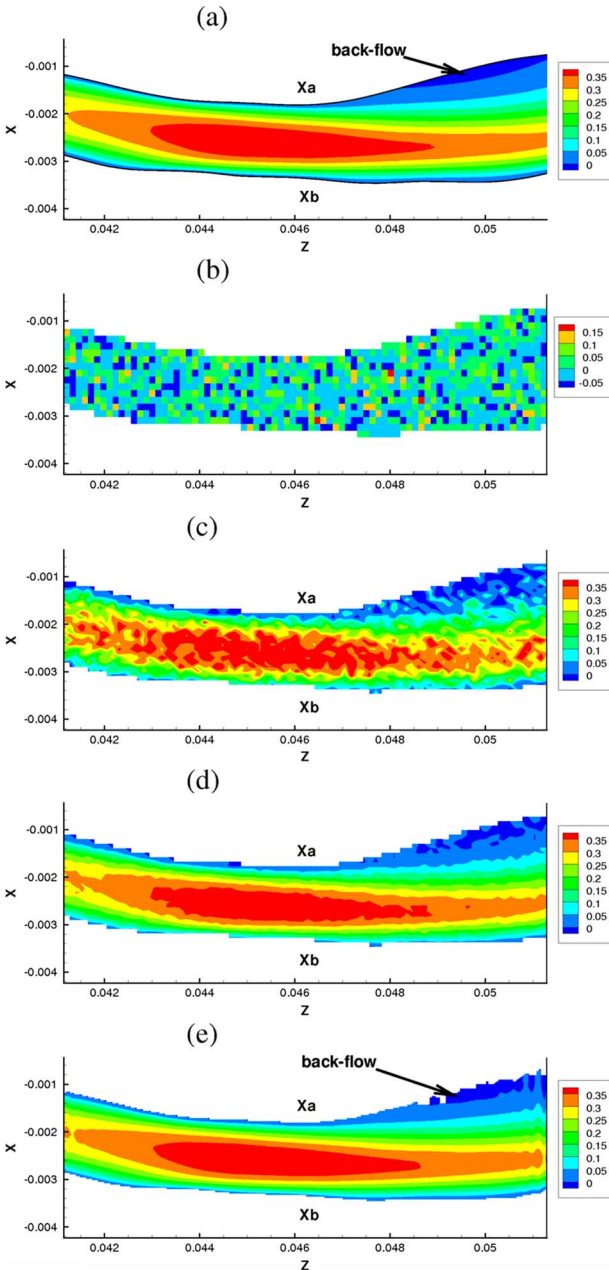


Fig. 16. Reconstruction of the axial w -velocity field from noisy data, $t = 0.2$; (a)—CFD; (b)—distribution of speckle noise; (c)—noisy data (ultrasound-like image); (d)—the image shown in (c) after ensemble averaging (still noisy); (e)—the image shown in (d) after POD-K.

struction so we present results for these instants. The two other time instants ($t = 0.59$ and 0.73) are inside the diastolic phase.

As seen in Figs. 9 and 10, increasing the resolution in the x direction improved the WSS on the Xb-boundary. Hence, in order to calculate the WSS for the noisy data, we used $\Delta x = 93 \mu\text{m}$. The results are sensitive to the set of parameters specified for smoothing and Kriging interpolation. The correlation parameters of the spline kernel in (21) were chosen to provide the best agreement with WSS of the CFD simulation. For comparison, we created a test case when 1) the CFD data is noise-free and 2) the parameters of Kriging are the same as those used for the noisy data. We refer to this case as “Kriging (noise-free)”. We

recall that for the noisy data the smoothing parameters were targeted to provide the maximum SNR, but here we use a different criterion as we focus on WSS.

Fig. 17 shows the WSS calculated after applying the POD-Kriging procedure for noisy ultrasound-like images. The agreement with the CFD-based WSS is very good except in the region $49 < z < 51$, where the velocity is very low and reverse flow possible near the upper Xa-boundary [see Fig. 16(a)]. The data scattering near the edge $z = 51$ indicates that Kriging interpolation and smoothing alone fail to completely recover the correct information there. We note, however, that the agreement with the “Kriging (noise-free)” case is excellent but on the Xb-boundary both results differ from the WSS obtained for a gappy data set shown in Fig. 10(b). This is attributed to the use of different correlation parameters (see Table V) employed for the gappy and noisy cases due to different optimization criteria. Relative errors are summarized in Table VI. Sensitivity of the results to different correlation parameters is shown in Table VII.

Kriging-based interpolation was used for finding from $\tilde{w}(x, z) = 0$ the vessel boundary shown in Fig. 18. For $t = 0.12$ and 0.2 , the agreement with the “true” (CFD) boundary is very good except in the low-velocity region. We note that similar comparisons performed for $t = 0.59$ and 0.73 shown excellent agreement.

IV. SUMMARY AND DISCUSSION

Advanced reconstruction of clinical images can significantly enhance the quality of images in cardiovascular medicine and also provide missing information in space or time. In this paper, we considered some prototype cases to reconstruct both *in time and space* gappy and noisy data in a carotid artery. The new reconstruction method we proposed is based on the principles of evolving dynamic systems and optimum statistical space interpolation. In particular, we propose to apply 1) POD for processing medical images collected over a time interval (snapshots), and 2) Kriging interpolation to black zones and to images with low resolution (i.e., at subpixel level). We found that for certain cases of practical interest combining both approaches (POD-K) yields the best performance for typical ultrasound-like images.

In particular, we aimed to systematically test and evaluate the effectiveness of the proposed reconstruction procedure. We have successfully applied the POD-Kriging method so far to limited clinical data (see example in Figure 1) but we could not evaluate the effectiveness of our method due to the lack of “true” data sets. To this end, in this paper we synthesized a prototype of clinical data from high-resolution CFD data sets with the velocity field data obtained from 3-D CFD simulations of flow through a carotid artery. Our major concern was to have reliable *accurate* numerical data sets to compare with. Admittedly, the Reynolds number in our simulations was relatively low for computational expedience since in the reconstruction process of the data sets considered in this paper only a few POD modes were required and this made our parametric study easier to complete. However, this does not mean that the method will fail for patient-specific data as it is general. For example, the presence of stenosis may trigger transition from laminar to turbulent flow in carotid artery even for flow with moderate Reynolds number.

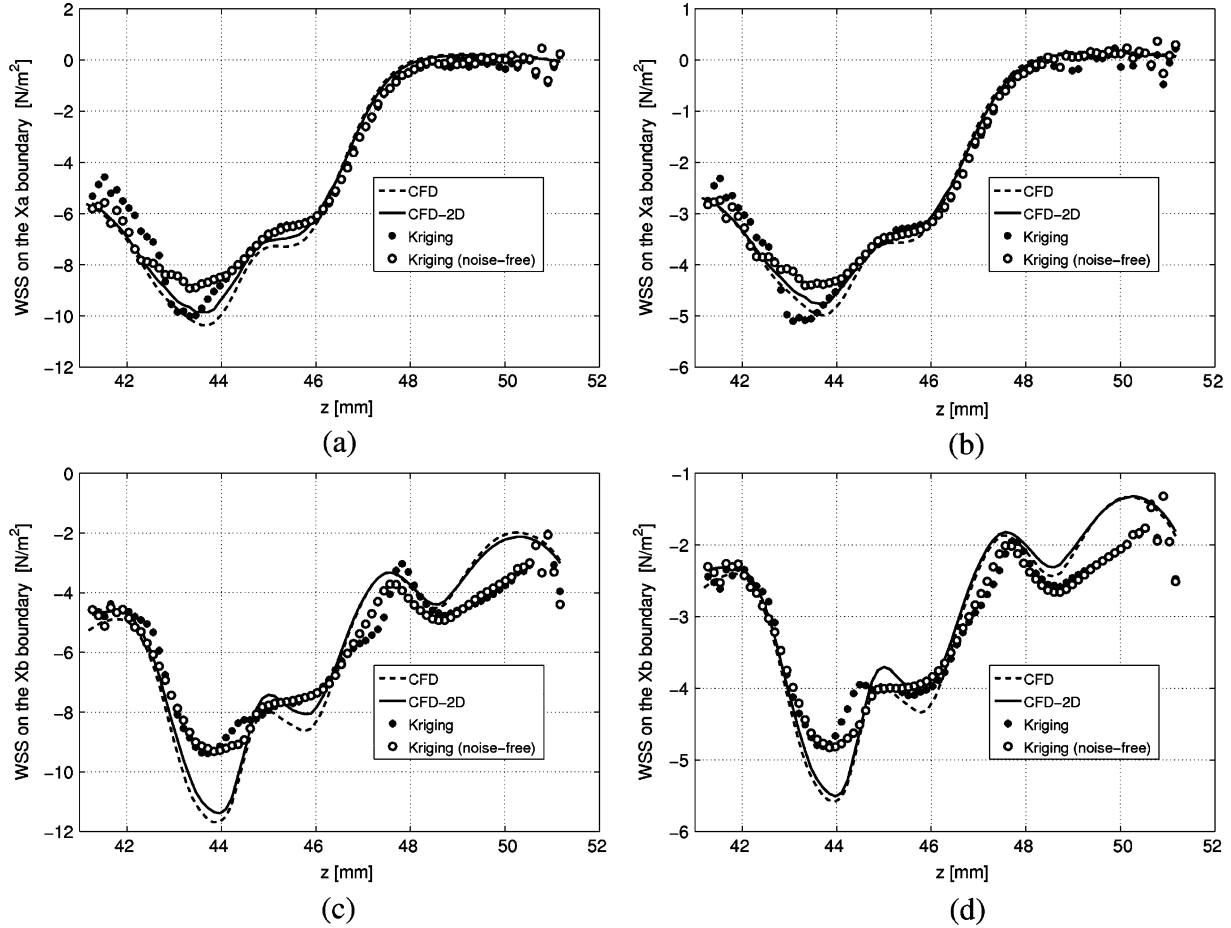


Fig. 17. Speckle noise, $\text{SNR} \approx 5$; spatial resolution $\Delta x = 93 \mu\text{m}$, $\Delta z = 130 \mu\text{m}$. Calculation of WSS at different time instants $t = 0.12$ (left) and $t = 0.2$ (right). The first row shows results for the upper boundary Xa and the second row results for the lower boundary Xb . (a) $t = 0.12$, (b) $t = 0.2$, (c) $t = 0.12$, (d) $t = 0.2$.

TABLE V
CORRELATION PARAMETERS OF KRIGING INTERPOLATION (SPLINE KERNEL)

Case	θ_x	θ_z
Noisy data	0.04	3
Gappy data (LRG)	0.03	2

TABLE VI
SPECKLE NOISE. RELATIVE ERRORS BETWEEN WSS COMPUTED ON $MESH_2$ AND THE "TRUE" WSS_{CFD-2D}

Boundary	$t=0.12$	$t=0.2$
Xa	8.5%	7.7%
Xb	13.4%	13.1%

TABLE VII
SPECKLE NOISE. COMPARISON OF RELATIVE ERRORS BETWEEN WSS AND THE "TRUE" WSS_{CFD-2D} FOR DIFFERENT CORRELATION PARAMETERS ($MESH_2$, $t = 0.2$)

θ_x	θ_z	Xa	Xb
0.01	3	9.1%	14.8%
0.04	3	7.7%	13.1%
0.1	3	10.0%	15.5%
0.04	2	8.2%	13.1%
0.04	4	8.0%	13.5%

In that case, the POD-based reconstruction is also possible but the number of modes needed for accurate reconstruction will be higher.

Our method treats medical images with spatio-temporal gappy (incomplete) and noisy data and can be applied in conjunction with other methods dealing with correction and possible elimination of artifacts [29]. In this study, spatio-temporal gappiness was first created by discarding some data points of the CFD simulation *at random*. This is supposed to mimic a CDUS image with artifacts, although in real CDUS the velocity data is intrinsically convolved with a point spread function and there are no values representing the velocity at grid points. Another possibility is to assign a specific *confidence level* at each data point, i.e., a weight between zero and one, the latter value corresponding to the case for which we know the point value of velocity *for sure*. This, however, requires additional information or assumptions that may complicate the comparative study we aimed for in the present work. To this end, our approach can be interpreted as a case with confidence levels of *zero* for the points discarded and *one* for the points for which we know the velocity values *for sure*. On the other hand, the creation of regions wherein the data are missing at all times—what we referred to as black zones—represents scenarios where no data are acquired there due to an obstructed view. We note that the POD method fails in the presence of a black zone but the Kriging procedure we employed is very effective in recovering the missing information.

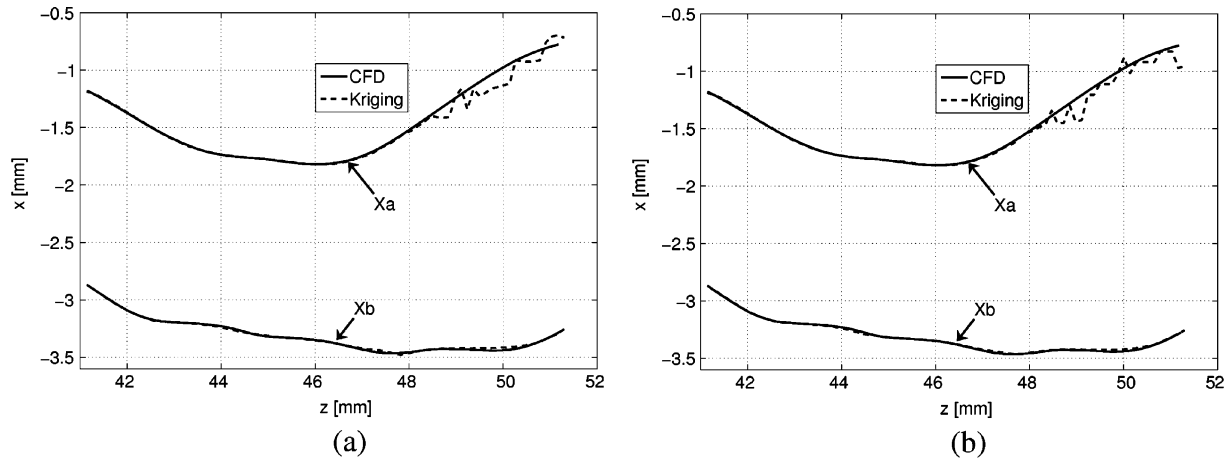


Fig. 18. Speckle noise, $\text{SNR} \approx 5$; spatial resolution $\Delta x = 93 \mu\text{m}$, $\Delta z = 130 \mu\text{m}$. Vessel boundaries obtained by Kriging interpolation at two different time instants. (a) $t = 0.12$, (b) $t = 0.2$.

TABLE VIII
SPECKLE NOISE. COMPARISON OF RELATIVE ERRORS BETWEEN
WSS COMPUTED FOR DIFFERENT INITIAL NOISE LEVELS

Initial SNR	WSS RMS on Xa	WSS RMS on Xb
5 (14 dB)	8.5%	13.4%
2.5 (8 dB)	9.2%	14.0%
1.3 (2.3 dB)	16.4%	16.8%

Finally, we injected “noise” explicitly to the CFD results to study its effect on the reconstruction. Sensitivity of the results to different initial SNR is shown in Table VIII. In brackets, we show the SNR values measured in decibels, $\text{SNR}_{\text{dB}} = 20 \log_{10} \text{SNR}$. In [36], the authors used initial $\text{SNR} = 3.16$ (10 dB). In the present work, we formed the *ensemble average* first, based on which we extracted the POD modes. A further smoothing of the temporal and spatial modes led to good results for the speckle noise considered. This method can be easily generalized to be more effective, especially in the case of images with pathological events. Let us revisit the noisy data case we considered in Section III-B. Having the ensemble of 101×30 stochastic fields we can perform a proper orthogonal decomposition for each snapshot (e.g., 101 times) to obtain up to 30 POD modes (every time), thus obtaining essentially a Karh unen-Lo eve representation of each snapshot [17], [21]. By examining the corresponding eigenspectrum of a specific snapshot, we may be able to characterize the type of noise, i.e., how correlated it is and if, indeed, represents a pathological event or it is simply due to measurement artifacts. The first mode is the *mean*, which can be interpreted as the *ensemble* or *phase averaging* over the 30 cardiac cycles, i.e., what we employed in the current work. However, depending on the specific scenario we can include more modes in the representation of each snapshot. The type of information contained in the high modes can be evaluated based on the corresponding eigenspectrum; for example, a fast decay of the eigenvalues would imply the higher modes contain correlated noise.

The proposed POD-Kriging method, with additional POD treatment for noisy images, bears great promise in clinical practice as it provides velocity quantification even in the presence of

incomplete information. In particular, an *analytical* description of the velocity field $\tilde{w}(x, z) = \mathbf{K}(w)$ can be used for 1) locating the vessel’s boundary from $\tilde{w}(x, z) = 0$ and 2) computing the WSS. We showed that even in the presence of noise and extreme gappiness with black zones, the agreement with the “true” WSS (obtained from the high-resolution CFD data) is good at low imaging resolution and it improves significantly with assuming modest advances in medical imaging resolution enhancement anticipated in the future.

APPENDIX

CFD SIMULATION OF BLOOD FLOW IN THE CAROTID ARTERY

A geometric model of the carotid artery was obtained from *in vivo* MRA images.³ In particular, MRA images of cross-sectional slices of the left CCA, ICA, and external carotid (ECA) arteries were acquired by a Genesis Signa scanner using a 3-D time-of-flight (TOF) sequence. The distance between the slices was 1.2 mm and a total of 145 images was acquired. In order to obtain the required contours, the cross-sectional views of MRA images were segmented using a prespecified threshold pixel intensity and pixels’ coordinates defining the vessel boundaries (i.e., pixels’ x, y, z coordinates) are extracted. After performing the boundary identification procedure on MRA images of CCA, ICA, and ECA, the contours of the vessel walls were smoothed as follows. For each slice, the boundary contour coordinates were transformed from a Cartesian (x, y) to a polar coordinates system (r, θ) . The curve $r(\theta)$ was smoothed using LOESS described in Section II-D. The 3-D curves, formed by the cross-sectional slice centers, were smoothed by applying LOESS as well.

The smoothed data set of cross-sectional contours were exported to SolidWorks (SolidWorks Corporation, Concord, MA). Lofting the two-dimensional smoothed contours in the proper order yields the 3-D geometric model. The geometrical model has been extended in the both inlet and outlet directions by circular sections in order to achieve perfectly smooth transition of the cross sections from circular to the actual geometry,

³Courtesy of Prof. M. Gomori, Hadassah Medical Center, Jerusalem, Israel.

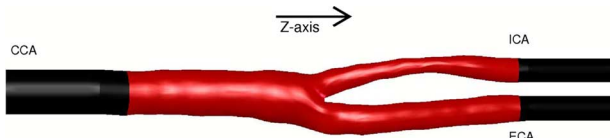


Fig. 19. Carotid artery obtained from *in vivo* MRA images.

TABLE IX
GEOMETRIC PARAMETERS OF THE CAROTID ARTERY

Model	Original	Extended
Total length, <i>mm</i>	42.3	65.1
Inflow section area - CCA, <i>mm</i> ²	17.4	17.4
Outflow section area - ICA, <i>mm</i> ²	4.8	4.8
Outflow section area - ECA, <i>mm</i> ²	5.4	5.4
Total volume, <i>mm</i> ³	610	943

TABLE X
COMPUTATIONAL MESH PARAMETERS. CCA; BR; ICA; ECA

Domain	Number of nodes
BR	24,413
CCA	181,102
ICA	176,902
ECA	156,128
Total	538,545

see Fig. 19. The modified geometry can readily accommodate fully-developed Womersley flow conditions. The parameters of this artery are summarized in Table IX and a 3-D perspective is shown in Fig. 19. The original geometry is in red while the extensions are in black.

The geometric model of the artery is then loaded to the mesh generator GAMBIT to generate the computational mesh, which is divided into four subdomains: 1) CCA, 2) bifurcation region (BR), 3) internal carotid (ICA), and 4) ECA arteries. A nonuniform mesh was used with elements clustering near the walls and in the regions with expected complex flow, e.g., bifurcation and stenosis. The CCA, ICA, and ECA subdomains are meshed by hexahedral mesh generation using the multiaxis Cooper's algorithm, while BR was meshed using tetrahedral volume meshes due to its structural complexity. The number of computational nodes in subdomains are summarized Table X.

We have employed two different approaches to perform CFD simulations at several resolutions of 3-D pulsatile flow through the carotid artery. The governing equations are the 3-D time-dependent Navier-Stokes (NS) equations, subjected to the incompressibility constraint. The simulations were performed based on the finite volume method using the commercial code Fluent (v6.2, Lebanon, New Hampshire). For verification purposes we also performed selective simulations using the code NEKTAR based on the spectral/*hp* element method [16]. We employed a mesh with 36 926 tetrahedral elements of polynomial order 4 and second-order time accurate integration. In all tested cases the difference in the velocity profiles obtained with the two methods was less than 2%.

The simulations were performed as follows. Starting from an arbitrary initial field a stationary limit cycle was achieved after ten cardiac cycles. With regards to boundary conditions, a Dirichlet condition based on the flow rate $Q(t)$ shown in Fig. 2

was used at the CCA inlet. This profile was approximated by $N = 30$ Fourier modes, i.e., $Q(t) = A_0 + \sum_{k=1}^N A_k \sin(k\omega t) + B_k \cos(k\omega t)$. Here ω is the main frequency and A_0, A_k, B_k are the coefficients of the Fourier expansion. A fully developed velocity profile was prescribed at the proximal end of the CC artery using superposition with the well-known Womersley analytical profile [34] for each Fourier mode of the flow rate curve. At the distal end of the IC and EC arteries, zero pressures were imposed. No-slip boundary conditions were prescribed at the vessel walls. In our simulations, the kinematic viscosity $\nu = 3.525 \text{ mm}^2/\text{s}$ and main frequency $\omega = 2\pi \text{ s}^{-1}$. The Reynolds number $\text{Re} = U_m D/\nu = 200$, where U_m is the peak systolic mean velocity, and D is the CCA inflow cross-section diameter; the Womersley number $W_o = 0.5D(\omega/\nu)^{1/2} = 3.1$.

ACKNOWLEDGMENT

The authors are deeply indebted to anonymous reviewers for the insightful comments that helped them to improve the quality and content of this paper and wish to express their appreciation to Dr. D. Venturi for valuable discussions.

REFERENCES

- [1] J. G. Abboti and F. L. Thurstone, "Acoustic speckle: Theory and experimental analysis," *Ultrason. Imag.*, vol. 1, pp. 303–324, 1979.
- [2] G. Bambi, T. Morganti, S. Ricci, E. Boni, F. Guidi, C. Palombo, and P. Tortoli, "A novel ultrasound instrument for investigation of arterial mechanics," *Ultrasonics*, vol. 42, pp. 731–737, 2004.
- [3] D. C. Barratt, B. Ariff, K. N. Humphries, S. A. Thom, and A. D. Hughes, "Reconstruction and quantification of the carotid artery bifurcation from 3-D ultrasound images," *IEEE Trans. Med. Imag.*, vol. 35, no. 5, pp. 567–583, May 2004.
- [4] V. Behar, D. Adam, and Z. Friedman, "A new method of ultrasound color flow mapping," *Ultrasonics*, vol. 41, pp. 385–395, 2003.
- [5] L. Bohs, S. Gebhart, and M. Anderson, "2-D motion estimation using two parallel receive beams," *IEEE Trans. Ultrason. Ferroelectr. Freq. Contr.*, vol. 48, no. 2, pp. 392–408, Mar. 2001.
- [6] P. J. Brands, A. P. G. Hoeks, L. Hofstra, and R. S. Reneman, "A noninvasive method to estimate wall shear rate using ultrasound," *Ultr. Med. Biol.*, vol. 21, pp. 171–185, 1995.
- [7] M. Calzolari, L. Capineri, A. Fort, L. Masotti, S. Rocchi, and M. Scabia, "A 3-D PW Ultrasonic doppler flow-meter: Theory and experimental characterization," *IEEE Trans. Ultrason. Ferroelectr. Freq. Contr.*, vol. 46, pp. 108–113, 1999.
- [8] C. G. Caro, J. M. Fitz-Gerald, and R. C. Schroter, "Atheroma and arterial wall shear: Observation, correlation and proposal of shear dependent mass transfer for atherogenesis," *Proc. R. Soc. Lond. B*, vol. 177, pp. 109–159, 1971.
- [9] W. S. Cleveland and S. J. Devlin, "Locally weighted regression: An approach to regression analysis by local fitting," *J. Am. Statist. Assoc.*, vol. 83, pp. 596–610, 1988.
- [10] R. M. Everson and L. Sirovich, "The Karhunen-Loève transform for incomplete data," *J. Opt. Soc. Am. A*, vol. 12, no. 8, pp. 1657–1664, 1995.
- [11] M. D. Fox and W. Cardiner, "Three-dimensional Doppler velocimetry of flow jets," *IEEE Trans. Biomed. Eng.*, vol. 35, no. 10, pp. 834–841, Oct. 1988.
- [12] D. P. Giddens, C. K. Zarins, and S. Glagov, "The role of fluid mechanics in the localization and detection of arteriosclerosis," *J. Biomech. Eng.*, vol. 115, pp. 588–594, 1993.
- [13] H. Gunes, S. Sirisup, and G. E. Karniadakis, "Gappy data: To Krig or not to Krig?," *J. Comp. Phys.*, vol. 212, pp. 358–382, 2006.
- [14] A. P. G. Hoeks, S. K. Samijo, P. J. Brands, and R. S. Reneman, "Non-invasive determination of shear-rate distribution across the arterial lumen," *Hypertension*, vol. 26, pp. 26–33, 1995.
- [15] P. Holmes, J. L. Lumley, and G. Berkooz, *Turbulence, Coherent Structures, Dynamical Systems and Symmetry*. Cambridge, U.K.: Cambridge Univ. Press, 1996.
- [16] G. E. Karniadakis and S. J. Sherwin, *Spectral/hp Element Methods for Computational Fluid Dynamics*. Oxford, U.K.: Oxford Univ. Press, 2005.

- [17] M. Kirby, *Geometric Data Analysis: An Empirical Approach to Dimensionality Reduction and the Study of Patterns*. New York: Wiley-Interscience, 2000.
- [18] U. Köhler, I. Marshall, M. B. Robertson, Q. Long, X. Xu, and P. R. Hoskins, "MRI measurements of the wall shear stress vectors in bifurcation models and comparison with CFD predictions," *J. Magn. Reson. Imag.*, vol. 14, pp. 563–573, 2001.
- [19] D. N. Ku, D. P. Giddens, C. K. Zarins, and S. Glagov, "Pulsatile flow and atherosclerosis in the human carotid bifurcation. Positive correlation between plaque location and low oscillating shear stress," *Arteriosclerosis*, vol. 5, pp. 293–302, 1985.
- [20] S. Lophaven, H. Nielsen, and J. Sondergaard, Informatics and mathematical modeling DTU, Rep. IMM-REP-2002-12, 2002.
- [21] M. Loève, *Probability Theory*, 4th ed. New York: Springer-Verlag, 1977.
- [22] A. Loupas, "Digital Image Processing for Noise Reduction in Medical Ultrasonics," Ph.D., Univ. Edinburgh, Edinburgh, U.K., 1988.
- [23] I. Marshall, S. Zhao, P. Papathanasopoulou, P. Hoskins, and X. Y. Xu, "MRI and CFD studies of pulsatile flow in healthy and stenosed carotid bifurcation models," *J. Biomech.*, vol. 37, pp. 679–687, 2004.
- [24] J. A. Moore, D. A. Steinman, and C. R. Ethier, "Computational blood flow modelling: Errors associated with reconstructing finite element models from magnetic resonance images," *J. Biomech.*, vol. 31, pp. 179–184, 1998.
- [25] S. Oyre, S. Ringgaard, S. Kozerke, W. P. Paaske, M. Erlandsen, P. Boesiger, and E. M. Pedersen, "Accurate noninvasive quantitation of blood flow, cross-sectional lumen vessel area and wall shear stress by three-dimensional paraboloid modeling of magnetic resonance imaging velocity data," *J. Amer. Col. Card.*, vol. 32, pp. 128–134, 1998.
- [26] P. Papathanasopoulou, S. Zhao, U. Köhler, M. B. Robertson, Q. Long, P. Hoskins, X. Y. Xu, and I. Marshall, "MRI measurement of time-resolved wall shear stress vectors in a carotid bifurcation model, and comparison with CFD predictions," *J. Magn. Res. Imag.*, vol. 17, pp. 153–162, 2003.
- [27] M. Sonka and J. Fitzpatrick, *Handbook of Medical Imaging, Medical Image Processing and Analysis*. Bellingham, WA: SPIE, 2000, vol. 2.
- [28] M. Stein, *Interpolation of spatial data: Theory for Kriging*. Berlin, Germany: Springer, 1999.
- [29] D. A. Steinman, C. R. Ethier, and B. K. Rutt, "Combined analysis of spatial and velocity displacement artifacts in phase contrast measurements of complex flows," *J. Magn. Res. Imag.*, vol. 7, pp. 339–346, 1997.
- [30] D. A. Steinman, J. B. Thomas, H. M. Ladak, J. S. Milner, B. K. Rutt, and J. D. Spence, "Reconstruction of carotid bifurcation hemodynamics and wall thickness using computational fluid dynamics and MRI," *Magn. Res. Med.*, vol. 47, pp. 149–59, 2002.
- [31] R. Stokholm, S. Oyre, S. Ringgaard, H. Flaagoy, W. P. Paaske, and E. M. Pedersen, "Determination of wall shear rate in the human carotid artery by magnetic resonance techniques," *Eur. J. Vasc. Endovasc. Surg.*, vol. 20, pp. 427–433, 2000.
- [32] J. Suzuki, R. Shimamoto, J. Nishikawa, T. Tomaru, T. Nakajima, F. Nakamura, W. S. Shin, and T. Toyo-oka, "Vector analysis of the hemodynamics of atherogenesis in the human thoracic aorta using MR velocity mapping," *Amer. J. Roentgenol.*, vol. 171, pp. 1285–1290, 1998.
- [33] D. Venturi and G. E. Karniadakis, "Gappy data and reconstruction procedures for flow past a cylinder," *J. Fluid Mechan.*, vol. 519, pp. 315–336, 2004.
- [34] F. M. White, *Viscous Fluid Flow*. New York: McGraw-Hill, 1991.
- [35] S. P. Wu, S. Ringgaard, and E. M. Pedersen, "Three-dimensional phase contrast velocity mapping acquisition improves wall shear stress estimation in vivo," *Magn. Res. Imag.*, vol. 22, pp. 345–351, 2004.
- [36] Y. Zhang, L. Wang, Y. Gao, J. Chen, and X. Shi, "Noise reduction in Doppler ultrasound signals using an adaptive decomposition algorithm," *Med. Eng. Phys.*, vol. 29, pp. 699–707, 2007.